



UNIVERSITY OF SUSSEX

1

DOCTORAL THESIS

2

⁴ Optimisation studies and background
⁵ estimation in searches for the supersymmetric
⁶ partner of the top quark in all-hadronic final
⁷ states with the ATLAS Detector at the LHC

8

9 *A thesis submitted in fulfillment of the requirements*
10 *for the degree of Doctor of Philosophy*

11

in the

12

Experimental Particle Physics Research Group

School of Mathematical and Physical Sciences

Author:

14

Fabrizio MIANO

Supervisor:

14

Dr. Fabrizio SALVATORE

15

2nd November 2017

Dedicated to my family.

*Have no fear for atomic energy
'cause none of them can stop the
time*

17

Robert Nesta Marley

18

Acknowledgments

- 19 Thanks to every single thing that went wrong. It made me stronger.

Declaration

21 I, Fabrizio MIANO, hereby declare that this thesis, titled, "Optimisation studies and back-
22 ground estimation in searches for the supersymmetric partner of the top quark in all-
23 hadronic final states with the ATLAS Detector at the LHC" has not been and will not be,
24 submitted in whole or in part to another University for the award of any other degree.

25 *Brighton, June 2018*

University of Sussex
School of Mathematical and Physical Sciences
Experimental Particle Physics Research Group

Doctoral Thesis

31
32 Optimisation studies and background estimation in searches for
33 the supersymmetric partner of the top quark in all-hadronic final
34 states with the ATLAS Detector at the LHC

36 by Fabrizio Miano

Abstract

38 This thesis presents searches for supersymmetry in $\sqrt{s} = 13$ TeV proton-proton collisions
39 at the LHC using data collected by the ATLAS detector in 2015, 2016 and 2017. Events
40 with 4 or more jets and missing transverse energy were selected. Kinematic variables were
41 investigated and optimisations were performed to increase the sensitivity to supersym-
42 metric signals. Standard Model backgrounds were estimated by means of Monte Carlo
43 simulations and data-driven techniques. Before analysing the data in the blinded signal
44 regions the agreement between data and background predictions and the extrapolations
45 from control and validation regions to signal regions were validated. The analysis yiel-
46 ded no significant excess in any of the analyses performed. Therefore limits were set and
47 the results were interpreted as lower bounds on the masses of supersymmetric particles
48 in various scenarios and models.

⁴⁹ Contents

⁵⁰	Introduction	1
⁵¹	1 The Standard Model, Supersymmetry, and the motivations behind it	2
⁵²	1.1 Overview	2
⁵³	1.2 Limitations of the Standard Model	8
⁵⁴	1.3 Supersymmetry	10
⁵⁵	1.3.1 Why SUSY?	11
⁵⁶	1.3.2 Third generation SUSY	13
⁵⁷	2 The ATLAS Experiment at the LHC	14
⁵⁸	2.1 The LHC	14
⁵⁹	2.2 The ATLAS Detector	16
⁶⁰	2.2.1 The Magnet System	18
⁶¹	2.2.2 The Inner Detector	19
⁶²	2.2.3 The Calorimeters	22
⁶³	2.2.4 The Muon Spectrometer	23
⁶⁴	2.3 The ATLAS Trigger System	24
⁶⁵	2.3.1 Level 1 Trigger	26
⁶⁶	2.3.2 High-Level Trigger	26
⁶⁷	3 The <i>b</i>-jet Trigger Signature in ATLAS	27
⁶⁸	3.1 Trigger Efficiency	27
⁶⁹	4 Event Simulation and Reconstruction	28
⁷⁰	4.1 Event Generation	28
⁷¹	4.1.1 Parton Distribution Functions (PDFs)	28
⁷²	4.1.2 Matrix Element Calculation	28
⁷³	4.1.3 Parton Showers	28

74	4.1.4 Hadronisation	28
75	4.2 Detector Simulation	28
76	5 Stop searches in final states with jets and missing transverse energy	29
77	6 Results and Statistical Intepretations	30
78	Trigger	31
79	Bibliography	32

⁸⁰ **List of Tables**

⁸¹	1.1 Forces and mediators described by the SM	5
⁸²	1.2 SUSY particles in the MSSM	12

⁸³ List of Figures

⁸⁴ 1.1	The Higgs potential in the complex plane.	8
⁸⁵ 1.2	Summary of several Standard Model total production cross section measurements, corrected for leptonic branching fractions, compared to the corresponding theoretical expectations. All theoretical expectations were calculated at NLO or higher. The luminosity used for each measurement is indicated close to the data point. Uncertainties for the theoretical predictions are quoted from the original ATLAS papers. They were not always evaluated using the same prescriptions for PDFs and scales. Not all measurements are statistically significant yet [1].	9
⁹³ 1.3	The inverse couplings of electromagnetic (dashed blue), weak (dashed red) and strong (solid green) interactions with the SM (left) and a supersymmetric model (right). In the SM the three lines do not meet at one point, but with the introduction of supersymmetry, and assuming that the supersymmetric particles are not heavier than about 1 TeV, they do meet. This is an indication that supersymmetry could be discovered at the LHC.	12
⁹⁹ 2.1	CERN Accelerator complex. The LHC is the last ring (dark grey line). Smaller machines are used for early-stage acceleration and also to provide beams for other experiments [2].	16
¹⁰² 2.2	Cut-away view of the ATLAS detector. The dimensions of the detector are 25 m in height and 44 m in length. The overall weight of the detector is approximately 7000 tonnes [2].	17
¹⁰⁵ 2.3	The ATLAS magnet system.	18
¹⁰⁶ 2.4	The ATLAS Inner Detector	20
¹⁰⁷ 2.5	A computer generated image of the full calorimeter.	22
¹⁰⁸ 2.6	Cut-away view of the ATLAS muon system [3].	24

109	2.7 The ATLAS TDAQ system. L1Topo and FTK were being commissioned	
110	during 2015 and not used for the results shown in this thesis [4].	25

111 Introduction

112 Last thing to write

¹¹³ **1** | ¹¹⁴ **The Standard Model, Supersym-**
¹¹⁵ **metry, and the motivations be-**
hind it

A theory is something nobody believes, except the person who made it. An experiment is something everybody believes, except the person who made it.

Albert Einstein

¹¹⁷ The Standard Model (SM) of particle physics is an effective theory that aims to provide
¹¹⁸ a general description of fundamental particles and the phenomena we see in nature, i. e.
¹¹⁹ the way they interact. Unfortunately, our understanding of nature is still limited due to
¹²⁰ some opened question to which the SM is not able to answer to, yet.

¹²¹ In this chapter, an overview of the SM will be presented in Section 1.1 together with
¹²² the limitations of such theory and some of the reasons behind the need of an extension.
¹²³ For the last decades theoretical physicsts have been trying to provide extensions to the
¹²⁴ SM, the so-called beyond-the-SM theories. Among these, one of the most popular, Super-
¹²⁵ symmetry which will be discussed in Section 1.3.

¹²⁶ **1.1 Overview**

¹²⁷ The 20th century can be considered a quantum revolution. Several experiments led to
¹²⁸ discoveries which were found to be, together with the formalised theory, a solid base of
¹²⁹ the Standard Model of particle physics and our description of nature. Several particles
¹³⁰ were predicted first by the SM and then experimentally observed e. g. the W and the Z

¹³¹ bosons, the τ lepton, [5], and more recently the Higgs boson at the LHC discovered by
¹³² ATLAS [6] and CMS [7].

¹³³ The SM lays on a Quantum Field Theory (QFT) where particles are treated like fields.
¹³⁴ It can describe three of the four fundamental forces; weak, electromagnetic, and strong.
¹³⁵ As of today, gravity is not considered in the SM. Sections 1.1 and 1.2 will be focused on
¹³⁶ the description of the fields together with the carriers of the information, and on the lim-
¹³⁷ itations that such theory implies, respectively.

¹³⁸ The most general classification of the particles within the SM can be made by means of
¹³⁹ spin. Fermions have half-integer spin values - and are usually referred to as matter -, and
¹⁴⁰ bosons have integer-spin values. A noteworthy subset of bosons is formed by the Spin-1
¹⁴¹ bosons (also known as gauge bosons). These can be considered the information carriers
¹⁴² or, in fact, the mediators of the forces.

¹⁴³ Fermions

¹⁴⁴ Six quarks and six leptons belong to the fermions family. In particular, fermions can be
¹⁴⁵ grouped into three generations. Each generation contains four particles; one up- and one
¹⁴⁶ down-type quark, one charged lepton and one neutral lepton. The masses of the charged
¹⁴⁷ leptons and quarks increase with the generation. The six quarks of the SM can be grouped
¹⁴⁸ into three doublets:

$$\begin{pmatrix} u \\ d \end{pmatrix}, \quad \begin{pmatrix} c \\ s \end{pmatrix}, \quad \begin{pmatrix} t \\ b \end{pmatrix}$$

¹⁴⁹ The up-type quarks (up, charm, top) have charge $+\frac{2}{3}e$ and the down-type quarks (down,
¹⁵⁰ strange, beauty/bottom) have charge $-\frac{1}{3}e$, where e is the electron charge. Quarks also
¹⁵¹ have another quantum number that can be seen as the analogue of the electric charge,
¹⁵² which is the colour charge. This can exist in three different states; "red", "green" and
¹⁵³ "blue". Moreover, as a consequence of *confinement*, which will be discussed later on in
¹⁵⁴ this section, quarks cannot exist as free particles. They rather group to form hadronic
¹⁵⁵ matter, also known as *hadrons*. There are two kinds of hadrons; mesons and baryons.
¹⁵⁶ Mesons are quark-antiquark systems, e.g. the pion, and baryons are three-quark system,
¹⁵⁷ e.g. protons and neutrons. Quarks and anti-quarks have a baryon number of $\frac{1}{3}$ and $-\frac{1}{3}$,
¹⁵⁸ respectively.

¹⁵⁹ There are six leptons and they can be classified in charged leptons (electron e , muon
¹⁶⁰ μ , tau τ) and neutral leptons (electron neutrino ν_e , muon neutrino ν_μ , tau neutrino ν_τ).

$$\begin{pmatrix} \nu_e \\ e^- \end{pmatrix}, \quad \begin{pmatrix} \nu_\mu \\ \mu^- \end{pmatrix}, \quad \begin{pmatrix} \nu_\tau \\ \tau^- \end{pmatrix}$$

161 Each lepton has a characteristic quantum number, called lepton number (L). Negatively
162 (positively) charged leptons have $L = -1$ ($L = 1$) and neutral leptons have $L = 0$. The
163 lepton number is conserved in all the interactions.

164 Forces of Nature

165 Forces in the SM are described by gauge theories, where the interactions is mediated by
166 a vector gauge boson.

167 The electromagnetic force is described by Quantum ElectroDynamics (QED) and, as
168 its mediator is the photon (γ) which couples to charged particles, it only affects charged
169 leptons and quarks, not neutrinos. They are instead affected by the weak force which is
170 mediated by the bosons W^\pm and Z^0 .

171 The weak interaction is associated with handedness (the projection of a particle spin
172 onto its direction of motion). Both leptons and quarks have left- and right-handed com-
173 ponents. However, only the left-handed (right-handed) component for neutrinos (anti-
174 neutrinos) has been observed. This means that nature prefers to produce left-handed
175 neutrinos and right-handed anti-neutrinos, which is the so-called parity violation.

176 The strong interactions, mediated by the gluon (electrically neutral and massless), is
177 described by Quantum ChromoDynamics (QCD). Its coupling increases with increasing
178 distance and is smaller at short range. Moreover, due to gluon self interactions, two
179 different phenomena arise; *confinement*: neither quarks nor gluons are observed as free
180 particles, but only colourless “singlet” states can be observed as “jets”, namely collim-
181 ated cone-shaped sprays of hadrons; *asymptotic freedom*: interactions between quarks and
182 gluons become weaker as the energy scale increases and the corresponding length scale
183 decreases.

184 Table 1.1 summarises the forces described in the SM and their mediators’ main char-
185 achteristics. Finally, the gravitational force, which is believed to be mediated by the grav-
186 iton, is not included in Table 1.1 as it is not part of the SM.

187 Symmetries and Gauge Groups

188 In 1915, the mathematician Emmy Noether (23 March 1882 – 14 April 1935) proved that
189 every differentiable symmetry of the action - defined as the integral over space of a Lag-

Table 1.1: Forces and mediators described by the SM

Force	Name	Symbol	Mass [GeV]	Charge
Electromagnetic	Photon	γ	0	0
Weak	W	W^\pm	80.398	$\pm e$
	Z	Z^0	91.188	0
Strong	Gluon	g	0	0

190 rangian density function - of a physical system has a corresponding conservation law.
191 More generally, a symmetry is a property of a physical system. Under certain transforma-
192 tions this property is preserved.

193 A gauge theory in QFT, is a theory in which the Lagrangian is invariant under a con-
194 tinuous group of local transformation. Group theory was then adopted to describe the
195 symmetries conserved in the SM. The gauge group of the theory is the *Lie Group*. It con-
196 tains all the transformations between possible gauges. The Lie algebra of group generators
197 is therefore associated with any Lie group and for each group generator there emerges a
198 corresponding field: the gauge field. The quanta of the gauge fields are called *gauge bo-*
199 *sons*.

200 The three SM interactions can therefore be mathematically described by the following:

$$U(1)_Y \otimes SU(2)_L \otimes SU(3)_C \quad (1.1)$$

201 Here, Y is the weak hypercharge, used to estimate the correlation between the electric
202 charge (Q) and the third component of the weak isospin (I_3) via the relation $Q = I_3 + Y/2$,
203 where I_3 can either be $\pm 1/2$ or 0 for left-handed and right-handed particles, respectively;
204 C the colour charge and L the left-handedness.

205 As of today, we can describe three of the four forces of nature with group theory. QED
206 is an Abelian gauge theory with $U(1)$ as symmetry group, with the electromagnetic four-
207 potential as its gauge field and with the photon as its gauge boson [8]. The interactions
208 between charged fermions occurs by the exchange of a massless photon.

209 The weak interaction and the strong interactions are non-Abelian gauge theories with
210 gauge groups $SU(2)$ and $SU(3)$, respectively. As a consequence of being non-Abelian
211 the generators commutators are non-vanishing and therefore the gauge bosons can self-
212 interact. The $SU(2)$ generators of the weak interaction are the massless gauge bosons
213 $W_\mu^{\alpha=1,\dots,3}$ and, as mentioned earlier on in this chapter, they violate the parity by acting
214 only on left-handed particles.

²¹⁵ The gauge bosons of $SU(3)_C$ are eight massless gluons, $G_\mu^{\alpha=1,\dots,8}$. The strong interaction
²¹⁶ does not distinguish left- and right-handed particles. Finally, the Quarks that interact
²¹⁷ through weak interaction are mixtures of SM eigenstates as described by the CKM matrix
²¹⁸ [9].

²¹⁹ Electroweak Symmetry Breaking and the Higgs mechanism

²²⁰ In 1979 Sheldon Glashow, Abdus Salam, and Steven Weinberg were awarded the Nobel
²²¹ Prize in Physics for their contributions to the so-called electroweak unification. In
²²² the mathematical description of the SM in 1.1 the electroweak interaction is described by
²²³ $U(1)_Y \otimes SU(2)_L$. The electroweak physical bosons W , Z and γ are related to the four
²²⁴ unphysical gauge bosons $W_\mu^{\alpha=1,\dots,3}$ and B_μ^0 . In particular, to obtain the physical bosons
²²⁵ the gauge bosons have to mix as follows:

$$\begin{pmatrix} A_\mu \\ Z_\mu \end{pmatrix} = \begin{pmatrix} \cos \theta_W & \sin \theta_W \\ -\sin \theta_W & \cos \theta_W \end{pmatrix} \begin{pmatrix} B_\mu \\ W_\mu^3 \end{pmatrix} \quad (1.2)$$

²²⁶ Here, θ_W is the so-called *Weinberg angle* which is the angle by which spontaneous sym-
²²⁷ metry breaking rotates the original W_μ^3 and B_μ , producing the physical Z , and the photon.
²²⁸ θ_W can be experimentally determined in terms of the coupling strengths of the $B_\mu(g_1)$ and
²²⁹ the $W_\mu^\alpha(g_2)$ to the fermions using the relation $\tan \theta_W = g_1/g_2$. The field mixing of gauge
²³⁰ bosons that gives birth to the physical ones can be mathematically expressed by the fol-
²³¹ lowing:

$$A_\mu = W_\mu^3 \sin \theta_W + B_\mu \cos \theta_W \quad (1.3)$$

²³²

$$Z_\mu = W_\mu^3 \cos \theta_W - B_\mu \sin \theta_W \quad (1.4)$$

²³³ where A_μ and Z_μ represent the photon and the Z boson, respectively. The charged vector
²³⁴ bosons, W_μ^\mp , and its complex conjugate are defined as:

$$W_\mu^\pm = \frac{1}{\sqrt{2}} (W_\mu^1 \mp iW_\mu^2) \quad (1.5)$$

²³⁵ Mass terms for both gauge bosons and fermionic fields are not invariant under gauge
²³⁶ transformations and are therefore forbidden by the electroweak gauge. Nonetheless, it is
²³⁷ proven by experiments that W and Z are massive [8], therefore the SM assumption only
²³⁸ holds if the electroweak symmetry is broken.

²³⁹ The SM Lagrangian can be written as the sum of the various Lagrangians describing
²⁴⁰ the three interactions and the masses of the elementary particles as follows:

$$\mathcal{L}_{\text{SM}} = \mathcal{L}_{\text{EWK}} + \mathcal{L}_{\text{QCD}} + \mathcal{L}_{\text{Mass}} \quad (1.6)$$

²⁴¹ In order for the SM Lagrangian to remain a renormalisable theory, mass terms ($\mathcal{L}_{\text{Mass}}$)
²⁴² cannot be inserted by hand. A mechanism, that can preserve the gauge symmetry in
²⁴³ the SM and, that can solve the inconsistency arisen from the mass difference between
²⁴⁴ the gauge bosons and the physical ones, is needed. A British theoretical physicist, Peter
²⁴⁵ Higgs (29 May 1929, Newcastle upon Tyne, UK), came up with a brilliant solution for
²⁴⁶ which he was awarded the 2013 Physics Nobel Prize. In the 1960s, Higgs proposed that
²⁴⁷ broken symmetry in electroweak theory could explain the origin of masses of elementary
²⁴⁸ particles, and in particular of W and Z bosons: the Higgs mechanism was given birth.
²⁴⁹ The mechanism introduces a scalar field, known as the Higgs field, thought to couple to
²⁵⁰ both massive fermions and bosons.

²⁵¹ In the SM the Higgs field is a doublet in $SU(2)$:

$$\phi = \begin{pmatrix} \phi^+ \\ \phi^0 \end{pmatrix} \quad (1.7)$$

²⁵² with ϕ^+ and ϕ^0 being generic complex fields:

$$\phi^+ = \frac{\phi_1 + i\phi_2}{\sqrt{2}}, \quad \phi^0 = \frac{\phi_3 + i\phi_4}{\sqrt{2}} \quad (1.8)$$

²⁵³ Consider a Lagrangian of the form:

$$\mathcal{L}_{\text{Higgs}} = (\partial_\mu \phi)^* (\partial^\mu \phi) - V(\phi) \quad (1.9)$$

²⁵⁴ Renormalizability and $SU(2)_L \otimes U(1)_Y$ invariance require the Higgs potential to be of the
²⁵⁵ following form:

$$V(\phi) = \mu^2 \phi^\dagger \phi + \lambda (\phi^\dagger \phi)^2 \quad (1.10)$$

²⁵⁶ Eq. 1.9 is the Higgs Lagrangian if ϕ is chosen to be the following:

$$\phi = \begin{pmatrix} \phi^+ \\ \phi^0 \end{pmatrix} = \begin{pmatrix} G^+ \\ \frac{1}{\sqrt{2}} (v + H + iG^0) \end{pmatrix}$$

257 Here, the complex scalar field G^\pm and the real scalar field G^0 correspond to Goldstone
 258 bosons, and the real scalar field H is the SM Higgs boson field [10]. These massless scalars
 259 are absorbed due to the gauge transformations by the electroweak gauge bosons of the SM:

$$\phi = \begin{pmatrix} \phi^+ \\ \phi^0 \end{pmatrix} = \begin{pmatrix} 0 \\ \frac{1}{\sqrt{2}}(v + H) \end{pmatrix} \quad (1.11)$$

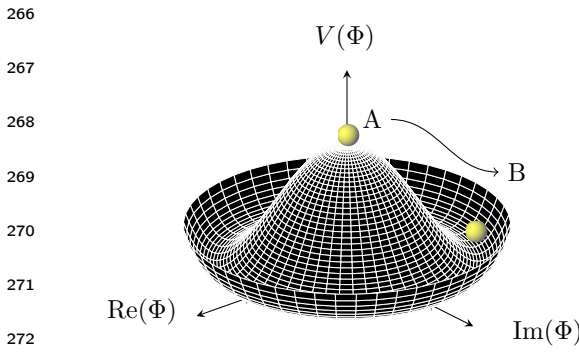
260 The Higgs potential in Eq. 1.10 is displayed in Fig. 1.1 if λ and μ are chosen to be
 261 real. Such potential has a non-zero ground state, v , also known as *vacuum expectation*
 262 *value* (VEV):

$$\phi_0 = \begin{pmatrix} 0 \\ \frac{1}{\sqrt{2}}v \end{pmatrix} \quad (1.12)$$

263 Such representation remains invariant under $U(1)$ allowing electric charge conservation.
 264 However, the SM gauge symmetry 1.1 is broken into $SU(2)_L \otimes U(1)_Y$.

265

In summary, to generate particle masses
 gauge symmetry must be broken. However, in order for the theory to remain
 renormalisable, the global Lagrangian
 symmetry must be preserved. This can be
 solved introducing the concept of *spontaneous*
symmetry breaking (SSB): a mechanism
 that allows a symmetric Lagrangian,
 but not a symmetric VEV. In particular,



274 Figure 1.1: The Higgs potential in the complex plane.

275 given a Lagrangian invariant under a cer-
 tain transformation, T_X and a generic set
 276 of states, that transform under T_X as the elements of a multiplet, the symmetry is spon-
 277 taneously broken if one of those states is arbitrarily chosen as the ground state of the sys-
 278 tem. The interaction of the Higgs field with the $SU(2) \otimes U(1)$ gauge fields, $W_\mu^\alpha = 1, 2, 3$,
 279 result in the three gauge bosons fields acquiring mass whilst the B_0 field stays massless.

280 1.2 Limitations of the Standard Model

281 During Run 1 and 2 of the LHC, the SM has been extensively validated, as shown in Fig.
 282 1.2: the agreement, between the measured production cross section of various SM pro-
 283 cesses and the SM predictions, looks very good. However, the reasons behind the mass

difference between the three generations of fermions are still not explained by the SM because masses are treated as free parameters of the theory. In addition, there are some fundamental questions that have still no answer and they will be briefly discussed this section.

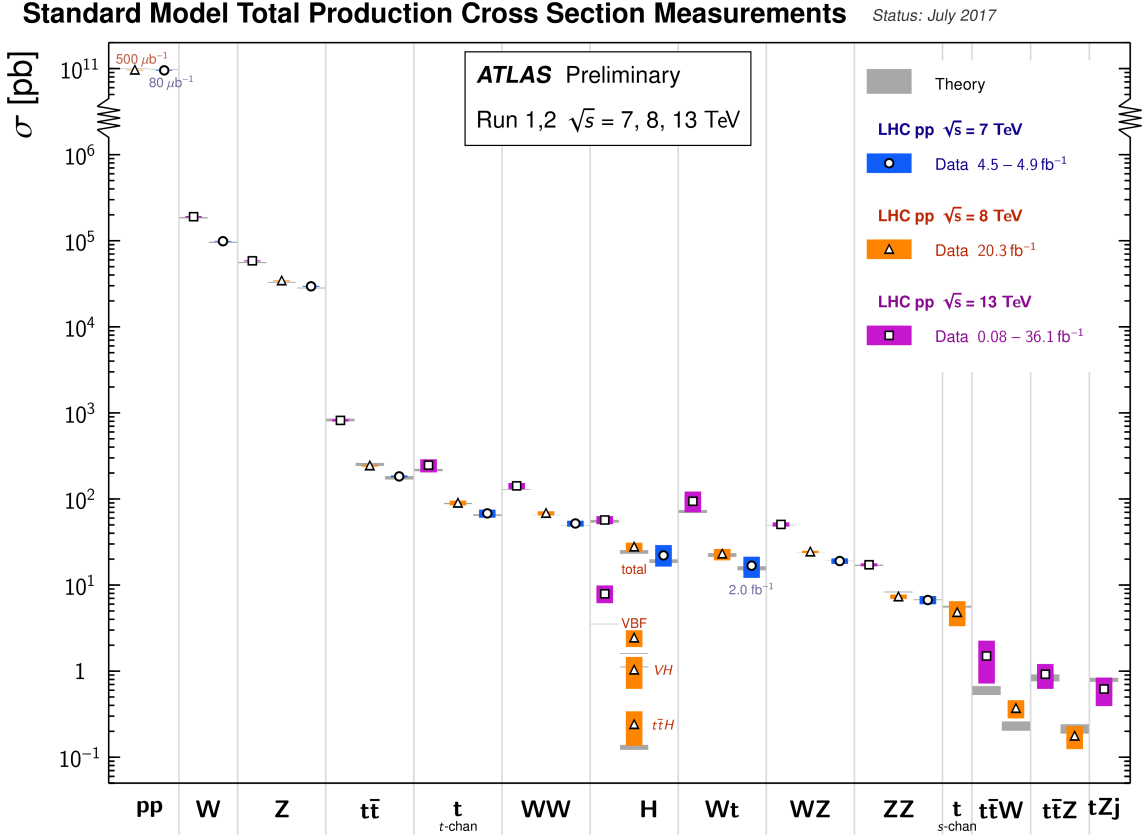


Figure 1.2: Summary of several Standard Model total production cross section measurements, corrected for leptonic branching fractions, compared to the corresponding theoretical expectations. All theoretical expectations were calculated at NLO or higher. The luminosity used for each measurement is indicated close to the data point. Uncertainties for the theoretical predictions are quoted from the original ATLAS papers. They were not always evaluated using the same prescriptions for PDFs and scales. Not all measurements are statistically significant yet [1].

288 Hierarchy Problem

Due to the coupling of the Higgs field to the fermionic fields the one-loop corrections to the Higgs mass receive several contributions. In particular:

$$\Delta m_H^2 = -\frac{|\lambda_f|^2}{8\pi^2} \Lambda_{\text{UV}}^2 + \dots \quad (1.13)$$

here, λ_f is the coupling constant to the fermionic field; Δm_H^2 is the difference between the observed Higgs mass m_H^2 and the bare mass, m_H^0 (Lagrangian parameter); Λ_{UV} is

²⁹³ the ultraviolet momentum cut-off, selected to be at the Planck scale ($\sim 2 \cdot 10^{18}$ GeV), at
²⁹⁴ which a QFT description of gravity is believed to become possible. The correction to the
²⁹⁵ Higgs mass then, will be around 30 orders of magnitude larger than Higgs mass itself,
²⁹⁶ in opposition to what has been measured. This difference just mentioned, between the
²⁹⁷ electroweak scale and the Planck scale arisen from the quantum corrections to the Higgs
²⁹⁸ mass, is the so-called Hierarchy Problem [11].

²⁹⁹ Neutrino Masses

³⁰⁰ The Super-Kamiokande Collaboration first, in 1998 [12], and SNO Collaboration later, in
³⁰¹ 2001 [13], have provided measurements of the neutrino flux from solar and atmospheric
³⁰² sources. The Nobel Prize in Physics 2015 was awarded jointly to Takaaki Kajita and Arthur
³⁰³ B. McDonald “for the discovery of neutrino oscillations, which shows that neutrinos have
³⁰⁴ mass” [14]. Such feature contradicts the absence of a mechanism for mass generation for
³⁰⁵ the neutrinos.

³⁰⁶ Various exotic solutions are on the market: one possible solution could be to add the
³⁰⁷ so-called Majorana mass terms for the neutrino (seesaw mechanism). Neutrino physics
³⁰⁸ could unveil physics beyond the SM.

³⁰⁹ Dark Matter

³¹⁰ Although dark matter (DM) has never been directly observed, its existence is inferred
³¹¹ from its gravitational effects. For example, looking at galaxies rotation, it was observed
³¹² that the rotation speed was higher than expected, given the amount of visible matter. Two
³¹³ different reasoning arose during the last century to justify such effect either there is matter
³¹⁴ that cannot be seen by us (in terms of visible light), which contributes to the galactic mass;
³¹⁵ or the general relativity works differently at galactic distances. The former is believed to
³¹⁶ be the most likely and it implies the existence of new particles which do not interact via
³¹⁷ electromagnetic interaction, the so-called Weakly Interacting Massive Particles (WIMPs).

³¹⁸ 1.3 Supersymmetry

³¹⁹ Supersymmetry links gravity with the other fundamental forces of nature by introducing
³²⁰ a space-time symmetry that relates bosons to fermions and vice-versa, via a transforma-

321 tion of the form of:

$$Q |\text{fermion}\rangle = |\text{boson}\rangle, \quad Q |\text{boson}\rangle = |\text{fermion}\rangle \quad (1.14)$$

322 For each SM particle there exists a superpartner with a spin difference of $\Delta s = 1/2$. As of
323 today, superpartners, generally called *sparticles* (where the *s* stands for “scalar”), have not
324 been observed yet, resulting in the assumption that SUSY must be a broken symmetry,
325 otherwise superpartners would have the same quantum numbers and masses as their
326 SM equivalent. However, if sparticles were to be too heavy (close to the Planck scale),
327 the hierarchy problem would still remain unsolved. The *soft* SUSY breaking mechanism
328 overcomes this problem imposing contrains on the masses of sparticles to a range that can
329 be experimentally explored.

330 In this section an overview of Supersymmetry (SUSY) will be presented, together with
331 the motivations behind the success of such theory. Third generation SUSY will be also
332 discussed as it is the most relevant theoretical support to the analyses presented in this
333 work.

334 1.3.1 Why SUSY?

335 One of the main motivations for SUSY is the cancellation of quadratic divergences to
336 Δm_H^2 . The introduction of SUSY particles with a half-integer spin difference with re-
337 spect to their SM provides a solution to the hierarchy problem. The Higgs mass squared
338 potential receives corrections from a new scalar of mass m_S of the form:

$$\Delta m_H^2 = -\frac{|\lambda_S|^2}{16\pi^2} \left[\Lambda_{\text{UV}}^2 - 2m_S^2 \ln(\Lambda_{\text{UV}}/m_S) + \dots \right] \quad (1.15)$$

339 where, λ_S is the coupling of SUSY particles to the Higgs field. This term cancels the
340 fermionic contributions in Eq. 1.13 since the couplings are the same. The experimental
341 value of Higgs mass will then not need any fine tuning.

342 Fig. 1.3 shows the inverse couplings as a function of the scale for both SM and the
343 Minimal Supersymmetric Standard Model (MSSM), which will be discussed in the next
344 paragraph. In the SM the three lines, representing electromagnetic (dashed blue), weak
345 (dashed red) and strong (solid green) interactions respectively, do not meet at one point,
346 but with the introduction of supersymmetry, and assuming that the supersymmetric particles
347 are not heavier than about 1 TeV, they do meet. This is an indication that supersymmetry
348 could be discovered at the LHC. The possible unification of the coupling constants at the
349 Planck scale is therefore another good motivation for SUSY searches.

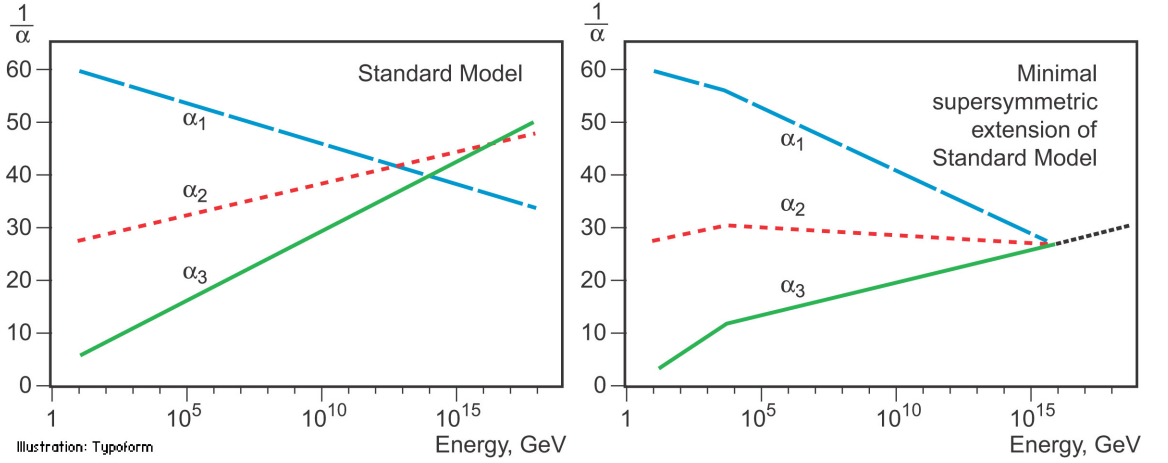


Figure 1.3: The inverse couplings of electromagnetic (dashed blue), weak (dashed red) and strong (solid green) interactions with the SM (left) and a supersymmetric model (right). In the SM the three lines do not meet at one point, but with the introduction of supersymmetry, and assuming that the supersymmetric particles are not heavier than about 1 TeV, they do meet. This is an indication that supersymmetry could be discovered at the LHC.

350 Minimal Supersymmetric Standard Model

351 The Minimal Supersymmetric Standard Model (MSSM), a minimal supersymmetric ex-
 352 tension of the SM [15], is defined by essentially doubling up the number of particles in
 353 the SM theory in order to include all the SM particles as well as their corresponding su-
 354 perpartners.

Table 1.2: SUSY particles in the MSSM

Name	Spin	Gauge Eigenstates	Mass Eigenstates
Squarks (\tilde{q})	0	$\tilde{u}_L \tilde{u}_R \tilde{d}_L \tilde{d}_R$	(same)
		$\tilde{c}_L \tilde{c}_R \tilde{s}_L \tilde{s}_R$	(same)
		$\tilde{t}_L \tilde{t}_R \tilde{b}_L \tilde{b}_R$	$\tilde{t}_1 \tilde{t}_2 \tilde{b}_1 \tilde{b}_2$
Sleptons (\tilde{l})	0	$\tilde{e}_L \tilde{e}_R \tilde{\nu}_L$	(same)
		$\tilde{\mu}_L \tilde{\mu}_R \tilde{\nu}_L$	(same)
		$\tilde{\tau}_L \tilde{\tau}_R \tilde{\nu}_\tau$	$\tilde{\tau}_1 \tilde{\tau}_2 \tilde{\nu}_\tau$
Higgs bosons	0	$H_u^0 H_d^0 H_u^+ H_d^-$	$h^0 H^0 A^0 H^\pm$
Neutralinos ($\tilde{\chi}_j^0$)	1/2	$\tilde{B}^0 \tilde{W}^0 \tilde{H}_u^0 \tilde{H}_d^0$	$\tilde{\chi}_1^0 \tilde{\chi}_2^0 \tilde{\chi}_3^0 \tilde{\chi}_4^0$
Charginos ($\tilde{\chi}_i^\pm$)	1/2	$\tilde{W}^\pm \tilde{H}_u^+ \tilde{H}_u^-$	$\tilde{\chi}_1^\pm \tilde{\chi}_2^\pm$
Gluino	1/2	\tilde{g}	(same)
Gravitino	3/2	\tilde{G}	(same)

355 Table 1.2 lists the MSSM particles. Scalar superpartners of quarks (leptons) are called
356 *squarks* \tilde{q} (*sleptons* \tilde{l}), short for “scalar quarks (leptons)” respectively. More generally they
357 are referred to as scalar fermions, or sfermions, \tilde{f} . A tilde above symbols is used to indicate
358 SUSY partners. As for gauge bosons and the Higgs, they have a fermionic superpartner.
359 These are referred to as *Gauginos* and *Higgsinos* and, differently from the SM, in the MSSM
360 there are two complex Higgs doublets:

$$H_u = (H_u^+, H_u^0) \quad H_d = (H_d^0, H_d^-)$$

361 with their respective VEVs, v_d , v_u which are constrained by the SM Higgs VEV:

$$v = \sqrt{v_u^2 + v_d^2}$$

362 Once electroweak symmetry is broken, eight degrees of freedom arise from the two Higgs
363 doublets. In particular, three of them give mass to the SM gauge bosons, W^\pm , Z , two for
364 charged Higgs bosons H^\pm and three for the three neutral Higgs bosons, h^0 (the lightest)
365 H^0 and A^0 . Winos, \tilde{W}^\pm , and Bino, \tilde{B}^0 mixing produce four neutralinos and four chargi-
366 nos, $\tilde{\chi}_i^0$ ($i = 1, 2, 3, 4$) and $\tilde{\chi}_{1,2}^\pm$, respectively. The mixing is described by equation 1.16 and
367 1.17 as it follows.

$$\begin{pmatrix} \tilde{\chi}_1^\pm \\ \tilde{\chi}_2^\pm \end{pmatrix} = \begin{pmatrix} M_2 & \sqrt{2}m_W \sin \beta \\ \sqrt{2}m_W \cos \beta & \mu \end{pmatrix} \begin{pmatrix} \tilde{W}^\pm \\ \tilde{H}^\pm \end{pmatrix} \quad (1.16)$$

$$\begin{pmatrix} \tilde{\chi}_1^0 \\ \tilde{\chi}_2^0 \\ \tilde{\chi}_3^0 \\ \tilde{\chi}_4^0 \end{pmatrix} = \begin{pmatrix} M_1 & 0 & -m_Z \cos \beta \sin \theta_W & -m_Z \cos \theta_W \sin \beta \\ 0 & M_2 & m_Z \cos \beta \cos \theta_W & m_Z \cos \theta_W \sin \beta \\ -m_Z \cos \beta \sin \theta_W & m_Z \cos \beta \sin \theta_W & 0 & -\mu \\ m_Z \sin \beta \cos \theta_W & m_Z \sin \beta \cos \theta_W & -\mu & 0 \end{pmatrix} \begin{pmatrix} \tilde{B}^0 \\ \tilde{W}^0 \\ \tilde{H}_u^0 \\ \tilde{H}_d^0 \end{pmatrix} \quad (1.17)$$

368 Here,

369 1.3.2 Third generation SUSY

³⁷⁰ 2 | The ATLAS Experiment at the ³⁷¹ LHC

³⁷² ATLAS (A Toroidal LHC ApparatuS) is one of the four main experiments (ATLAS, CMS,
³⁷³ ALICE, LHCb) taking data at a center-of-mass energy of 13 TeV using beams delivered by
³⁷⁴ the Large Hadron Collider (LHC). In this chapter an overview of the LHC will be given
³⁷⁵ in Section 2.1, then the ATLAS detector will be described in Section 2.2, and finally the
³⁷⁶ Trigger system, used to cleverly store the data, will be described in Section 2.3. A more
³⁷⁷ in-depth description of the Trigger algorithms I have been involved in will be given in
³⁷⁸ Chapter 3.

³⁷⁹ 2.1 The LHC

³⁸⁰ As of today, the LHC is the world's largest and most powerful particle accelerator. It was
³⁸¹ designed to help answer some of the fundamental open questions in particle physics by
³⁸² colliding protons at an unprecedented energy and luminosity. It is located at the European
³⁸³ Organisation for Nuclear Research (CERN), in the Geneva area, at a depth ranging from
³⁸⁴ 50 to 175 metres underground. It consists of a 27-kilometre ring made of superconducting
³⁸⁵ magnets, and inside it two high-energy particle beams travel in opposite directions and
³⁸⁶ in separate beam pipes.

³⁸⁷ The beams are guided around the ring by a strong magnetic field generated by coils -
³⁸⁸ made of special electric cables - that can operate in a superconducting regime. 1232 super-
³⁸⁹ conducting dipole and 392 quadrupole magnets, with an average magnetic field of 8.3 T,
³⁹⁰ are employed and kept at a temperature below 1.7 K, in order to preserve their supercon-
³⁹¹ ducting properties. The formers are used to bend the beams and the latters to keep them
³⁹² focused while they get accelerated.

³⁹³ The collider first went live on September 2008 even though, due to a magnet quench
³⁹⁴ incident that damaged over 50 superconducting magnets, it has been operational since

³⁹⁵ November 2009 when low-energy beams circulated in the tunnel for the first time since the
³⁹⁶ incident. This also marked the start of the main research programme and the beginning
³⁹⁷ of the so-called Run 1: first operational run (2009 - 2013).

³⁹⁸ Performance of the LHC

³⁹⁹ In June 2015 the LHC restarted delivering physics data, after a two-year break, the so-
⁴⁰⁰ called Long Shutdown 1 (LS1), during which the magnets were upgraded to handle the
⁴⁰¹ current required to circulate 7-TeV beams. It was the beginning of the so-called Run 2 -
⁴⁰² second operational run (2015-2018) - during which LHC has collided up to 10^{11} bunches
⁴⁰³ of protons every 25 ns at the design luminosity - the highest luminosity the detector was
⁴⁰⁴ designed to cope with - of $2 \cdot 10^{34} \text{ cm}^{-2} \text{s}^{-1}$. The definition of the luminosity is:

$$\mathcal{L} = f \frac{n_b N_1 N_2}{4\pi \sigma_x \sigma_y} \quad (2.1)$$

⁴⁰⁵ where N_1 and N_2 are the number of protons per bunch in each of the colliding beams, f
⁴⁰⁶ is the revolution frequency of the bunch collisions, n_b the number of proton per bunch,
⁴⁰⁷ and σ_x and σ_y are the horizontal and vertical dimensions of the beam. The luminosity is
⁴⁰⁸ strictly related to the number of collisions occurring during a certain experiment via the
⁴⁰⁹ following:

$$\mathcal{N}_{\text{event}} = \mathcal{L} \sigma_{\text{event}} \quad (2.2)$$

⁴¹⁰ where σ_{event} is the cross section of the process under investigation. It has not only collided
⁴¹¹ protons but also heavy ions, in particular lead nuclei at $\sqrt{s_{NN}} = 5.02 \text{ TeV}$, at a luminosity
⁴¹² of $10^{27} \text{ cm}^{-2} \text{s}^{-1}$ [16].

⁴¹³ Acceleration stages

⁴¹⁴ Before reaching the maximum energy, the proton beams are accelerated by smaller ac-
⁴¹⁵ celerators through various stages. Figure 2.1 shows a sketch of the CERN's accelerator
⁴¹⁶ complex. It all begins at the linear accelerator LINAC 2. Here protons are accelerated up
⁴¹⁷ to 50 MeV, and then injected in the Proton Synchrotron Booster (PSB) where they reach
⁴¹⁸ 1.4 GeV. The next stage is the Proton Synchrotron (PS), which boosts the beams up to 25
⁴¹⁹ GeV and then the Super Proton Synchrotron (SPS) makes them reach energies up to 450
⁴²⁰ GeV. Eventually, the beams are injected in bunches with a 25 ns spacing into the LHC,
⁴²¹ where they travel in opposite directions, while they are accelerated to up to 13 TeV. Once

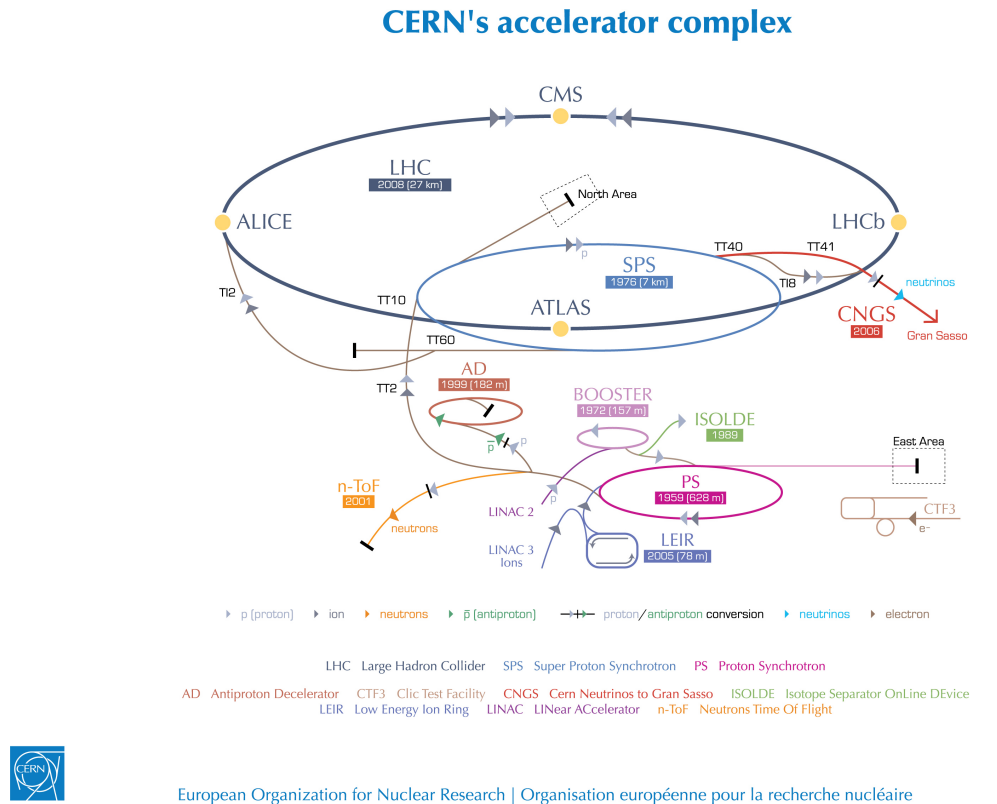


Figure 2.1: CERN Accelerator complex. The LHC is the last ring (dark grey line). Smaller machines are used for early-stage acceleration and also to provide beams for other experiments [2].

422 the bunches reach the maximum energy, they are made collide at four different points,
 423 inside four experiments around the ring [17].

424 The heavy ion beams acceleration procedure is slightly different. Their journey starts
 425 at LINAC 3 first, and the Low Energy Ion Ring (LEIR) then, before they make their way
 426 into the PS where they follow the same path as the protons [17].

427 The four large detectors on the collision points are; the multi-purpose detectors A Tor-
 428 oidal LHC ApparatuS (ATLAS), and Compact Muon Solenoid (CMS) [18], Large Hadron
 429 Collider beauty (LHCb) [19], which focuses on flavour physics, and A Large Ion Collider
 430 Experiment (ALICE) [20] which specialises in heavy ion physics. The *big four* are not the
 431 only experiments at the CERN's accelerator complex. There also are smaller experiments
 432 based at the the four caverns about the collision points e.g. TOTEM, LHCf and MoEDAL,
 433 but this will not be discussed any further in this thesis.

434 2.2 The ATLAS Detector

435 ATLAS is a general-purpose detector designed to collect data with the highest luminosity
 436 provided by the LHC. It is located at CERN's Point 1 cavern and it measures about 45 m in

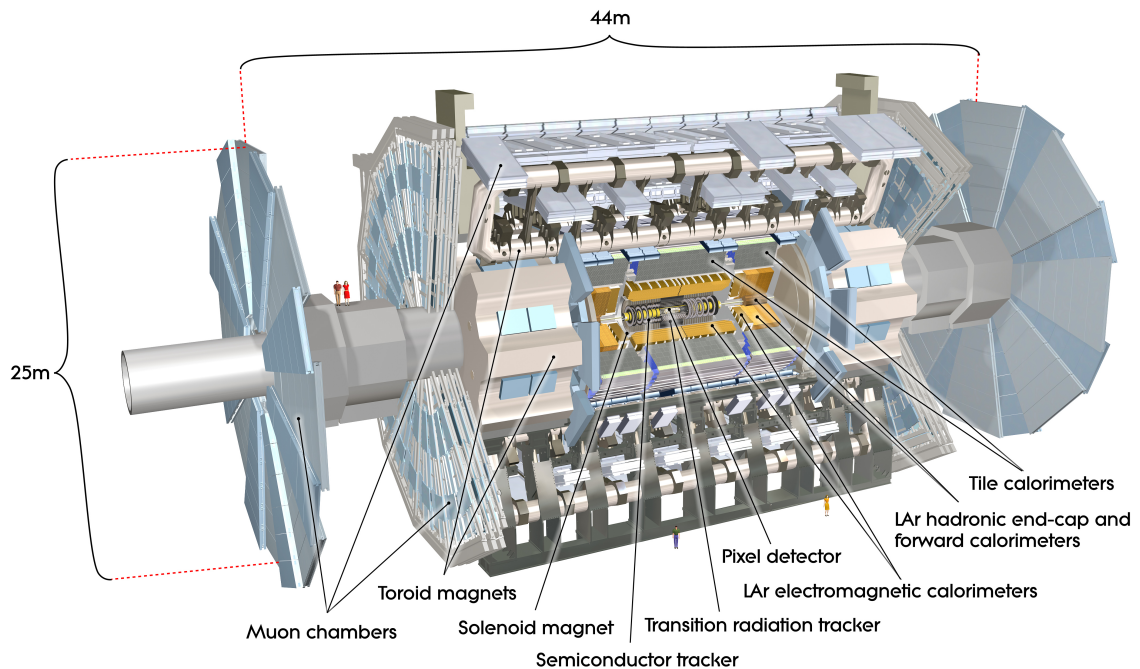


Figure 2.2: Cut-away view of the ATLAS detector. The dimensions of the detector are 25 m in height and 44 m in length. The overall weight of the detector is approximately 7000 tonnes [2].

length and 25 m in diameter. It has a forward-backward symmetric cylindrical geometry with respect to the interaction point and it is designed to reconstruct and measure physics objects such as electrons, muons, photons and hadronic jets. Its design was optimised to be as sensitive as possible to the discovery of the Higgs boson and beyond-the-Standard-Model (BSM) physics. In fact, thanks to the other sub-systems, ATLAS is able to observe all possible decay products by covering nearly 4π steradians of solid angle.

In Figure 2.2 a cut-away view of ATLAS with all its components is shown. The inner-most layer is the Inner Detector (ID) which is the core of the tracking system and consists of a Pixel, a Silicon micro-strip tracker (SCT), and a Transition Radiation Tracker (TRT). It is submerged in a 2 T magnetic field, generated by a thin superconducting solenoid, which bends all the charged particles' trajectories allowing transverse momentum measurement. The electromagnetic and hadronic calorimeters form the next layer and they are both used to perform precise energy measurements of photons, electrons, and hadronic jets. Finally, the outermost layer corresponds to the Muon Spectrometer (MS) which, together with the ID, enclosed in a toroidal magnetic field, allows precise measurement of momentum and position of muons. These sub-detectors will be discussed in more detail in the following sections.

454 The ATLAS coordinate system

455 A coordinate system is taken on for the spatial definition of the sub-systems and kinematic
 456 measurement of physics processes. Such system is defined starting from the interaction
 457 point, defined as the origin. The z -axis is defined by the beam direction and the $x - y$
 458 plan, as transverse to the beam direction.

459 A quantity, known as pseudorapidity, (η), is defined to describe the angle of a particle
 460 coming out of the collision, with respect to the beam axis:

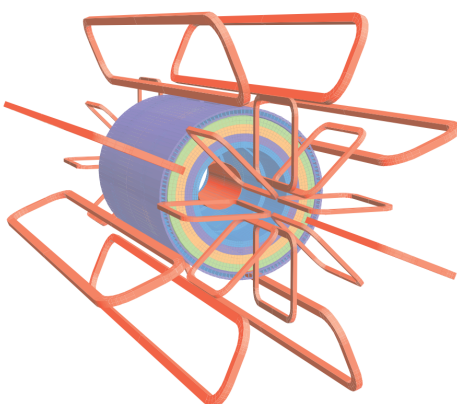
$$\eta \equiv -\ln(\tan(\theta/2))$$

461 Here θ is the polar angle. The azimuthal angle, ϕ , is defined around the beam axis and
 462 the polar angle. In the (η, ϕ) space a distance ΔR can be therefore defined as

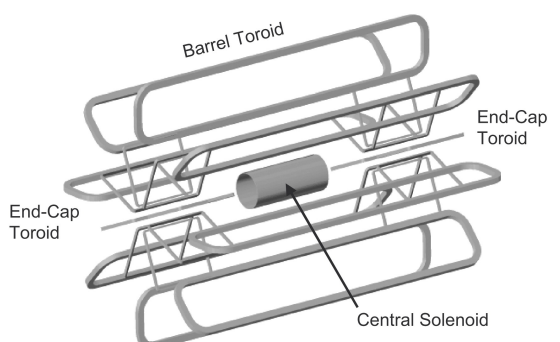
$$\Delta R = \sqrt{\Delta\eta^2 + \Delta\phi^2}$$

463 where $\Delta\eta$ and $\Delta\phi$ are the differences in pseudorapidity and azimuthal angle between any
 464 two considered objects. A central and a forward region of pseudorapidity are also defined
 465 such that the detector components are described as part of the *barrel* if they belong to the
 466 former or as part of the *end-caps* if they belong to the latter.

467 2.2.1 The Magnet System



(a) Geometry of magnet windings and tile calorimeter steel. The eight barrel toroid coils, with the end-cap coils interleaved are visible. The solenoid winding lies inside the calorimeter volume [3].



(b) Schematic view of the superconducting magnets [21].

Figure 2.3: The ATLAS magnet system.

468 The ATLAS magnet system, 26 m long with a 22 m diameter, generates the magnetic field
 469 needed to bend the trajectories of charged particles in order to perform momentum meas-
 470 urement. Figure 2.3a and 2.3b show the geometry of the system and its components,
 471 which are made of NbTi - superconducting material - and will be described in the follow-
 472 ing paragraphs.

473 **The Central Solenoid**

474 With an axial length of 5.8 m, an inner radius of 2.46 m, and an outer radius of 2.56 m, the
 475 central solenoid magnet is located between the ID and the ECAL. Its function is to bend
 476 the charged particles that go through the ID and it is aligned on the beam axis providing
 477 a 2 T axial magnetic field that allows accurate momentum measurement up to 100 GeV
 478 [21].

479 **The Barrel and the End-cap Toroids**

480 Figure 2.3b displays the toroid magnetic system that surrounds the calorimeters. With its
 481 cylindrical shape this component consists of a barrel and two end-caps toroids, each with
 482 eight superconducting coils. The system allows accurate measurement of muon momenta
 483 using a magnetic field of approximately 0.5 T (barrel) for the central regions and 1 T (end-
 484 cap) for the end-cap regions, respectively, which bends the particles in the θ direction.

485 **2.2.2 The Inner Detector**

486 The Inner Detector (ID) [22] is the innermost component of the ATLAS detector i. e. the
 487 nearest sub-detector to the interaction region and it is used to reconstruct charged particle
 488 tracks used in the selection of physics objects. In fact, it allows robust track reconstruction,
 489 with accurate impact parameter resolution ($\sim 20\mu m$) and precise primary and secondary
 490 vertex reconstruction for charged particles (tracks) above 500 MeV and within $|\eta| < 2.5$.

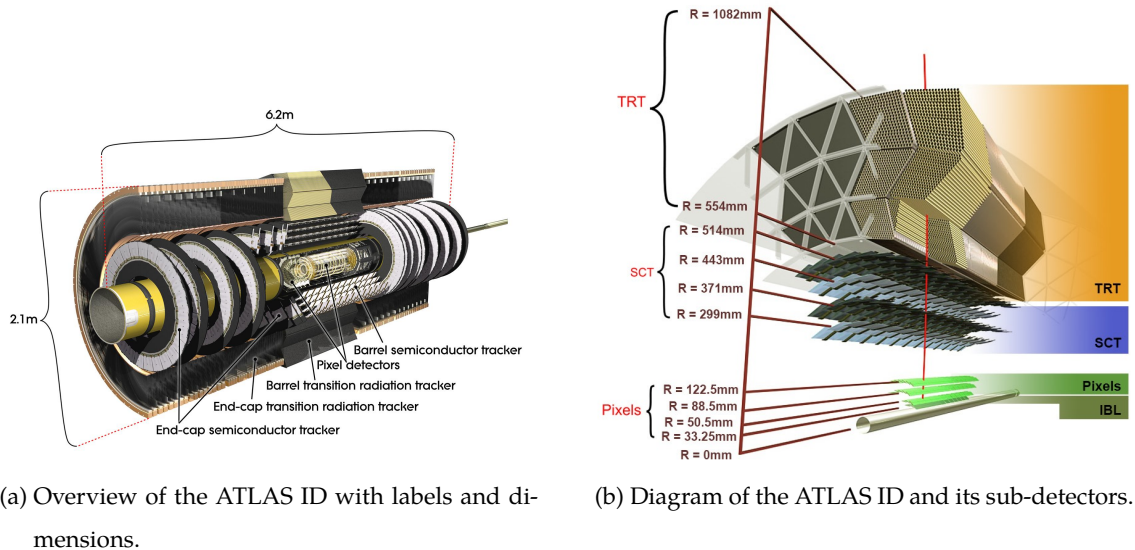
491 The ID is comprised of independent and concentric sub-systems, which are all shown
 492 in Figure 2.4:

- 493 • Insertable B-Layer (IBL):

494 innermost Pixel Detector layer added during ATLAS Run 2 upgrade (2013/2014) to
 495 improve vertexing and impact parameter reconstruction;

- 496 • Silicon Pixel Tracker (Pixel):

497 made of silicon pixel layers and used mainly for reconstructing both the primary



(a) Overview of the ATLAS ID with labels and dimensions.

(b) Diagram of the ATLAS ID and its sub-detectors.

Figure 2.4: The ATLAS Inner Detector

498 and secondary vertices in an event;

499 • SemiConductor Tracker (SCT):

500 comprised of silicon microstrip layers; thanks to its resolution ($17 \times 580 \mu\text{m}$) it can
501 accurately measure particle momenta;

502 • Transition Radiation Tracker (TRT):

503 final layer comprised of various layers of gaseous straw tube elements surrounded
504 by transition radiation material.

505 These sub-detectors will be discussed in the following sections.

506 **IBL**

507 The IBL [23] is the innermost Pixel Detector layer as shown in Figure 2.4b. It is comprised
508 of 6M channels and each pixel measures $50 \times 250 \mu\text{m}$. Its resolution is $8 \times 40 \mu\text{m}$,
509 addition of this new layer brought a considerable improvement on the performance of the
510 Pixel Detector by enhancing the quality of impact parameter reconstruction of tracks. In
511 particular, this was achieved by improving the vertex finding efficiency and the tagging
512 of bottom-quark-initiated jets (b -jets) which, in case of a B-layer failure, can be restored
513 by the IBL. Besides these improvements, the IBL insertion allowed ATLAS to better cope
514 with high luminosity effects such as the increase in event pile-up, which leads to high
515 occupancy and read-out inefficiency.

516 Pixel

517 The Pixel detector is comprised of 1750 identical sensorchip-hybrid modules, each cover-
 518 ing an active area of 16.4×60.8 mm. The total number of modules correspond to roughly
 519 80 million semiconductor silicon pixels. The nominal pixel size is $50 \mu\text{m}$ in the ϕ direction
 520 and $400 \mu\text{m}$ in the barrel region, along the z -axis (beam axis) [24]. The reason why such a
 521 large amount of pixels is employed is justified by the need to cope with the high luminos-
 522 ity in ATLAS. The silicon pixel detector measures 48.4 cm in diameter and 6.2 m in length
 523 providing a pseudorapidity coverage of $|\eta| < 2.5$. Figure 2.4b shows the three concentric
 524 barrel layers placed at 50.5 mm, 88.5 mm and 122.5 mm respectively. Furthermore, the
 525 Pixel detector is made of six disk layers, three for each forward region, such that when a
 526 charged particle crosses the layers it will generate a signal at least in three space points.
 527 The fine granularity of such detector allows accurate measurement and precise vertex re-
 528 construction, as it provides a more accurate position measurement as a large detection
 529 area is available. In particular, it has a resolution of $10 \times 115 \mu\text{m}$.

530 SCT

531 The SCT is made of 4088 modules of silicon micro-strip detectors arranged in four con-
 532 centric barrel layers. It is mainly used for precise momentum reconstruction over a range
 533 $|\eta| < 2.5$ and it was designed for precision measurement of the position using four points
 534 (corresponding to eight silicon layers), obtained as track hits when crossing the layers.
 535 Figure 2.4b shows the structure of the SCT with its four concentric barrel layers with radii
 536 ranging from 299 mm to 514 mm and two end-cap layers. Each module has an intrinsic
 537 resolution of $17 \mu\text{m}$ in the $R - \phi$ direction and $580 \mu\text{m}$ in the z direction. As the SCT is fur-
 538 ther away from the beam-pipe than the Pixel detector, it has to cope with reduced particle
 539 density. This allows for reduced granularity maintaining the same level of performance of
 540 the Pixel detector: SCT can use ~ 6.3 million read-out channels.

541 TRT

542 The last and outermost of the sub-systems in the ID is the TRT. It is a gaseous detector
 543 which consists of 4 mm diameter straw tubes wound from a multilayer film reinforced
 544 with carbon fibers and containing a $30 \mu\text{m}$ gold plated tungsten wire in the center. The
 545 straw is filled with a gas mixture of 70% Xe, 27% CO₂ and 3% O₂ [25]. As shown in Figure
 546 2.4b, its section consists of three concentric layers with radii ranging from 544 mm to 1082
 547 mm, each of which has 32 modules containing approximately 50,000 straws, 1.44 m in

length, aligned parallel to the beam direction with independent read-out at both ends.
 Both end-cap sections are divided into 14 wheels, with roughly 320,000 straws in the R-direction. The average 36 hits per track in the central region of the TRT allow continuous tracking to enhance pattern recognition and momentum resolution in the $|\eta| < 2.5$ region.
 It also improves the p_T resolution for longer tracks.

2.2.3 The Calorimeters

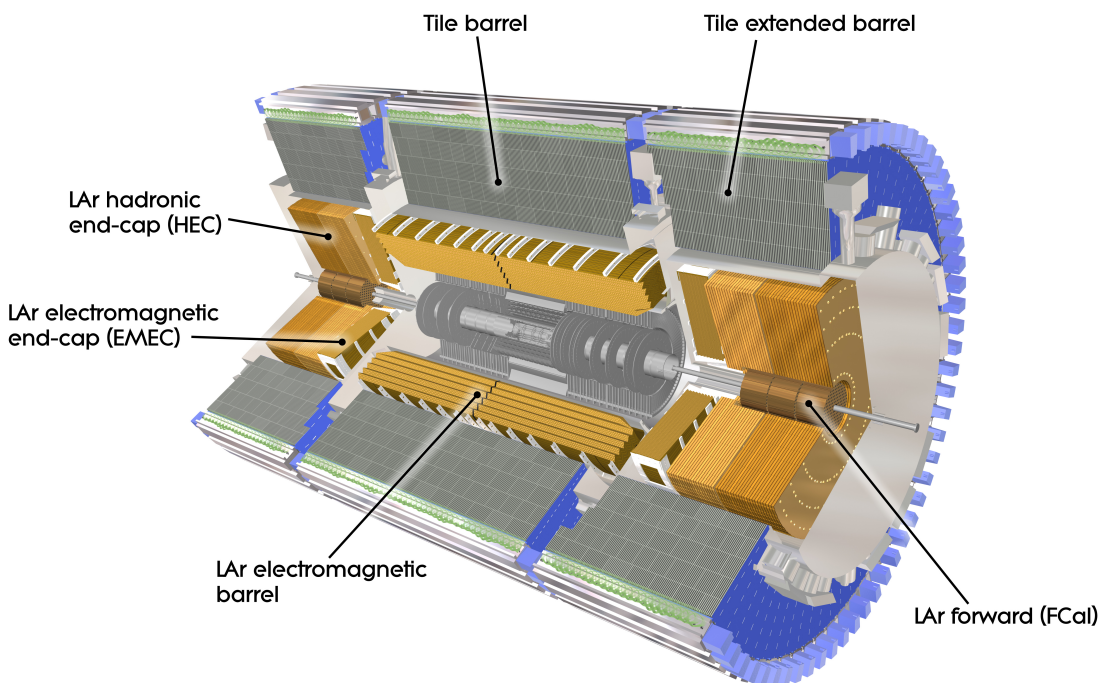


Figure 2.5: A computer generated image of the full calorimeter.

The ATLAS Calorimeter system, shown in Figure 2.5, is comprised of two main subsystems; the electromagnetic calorimeter (ECAL) and hadronic calorimeter (HCAL), which are designed to stop and measure the energy of electromagnetic-interacting and hadronic particles respectively. The combination of the two provides full coverage in ϕ and $|\eta| < 4.95$. Particles slow down and lose energy generating showers when crossing different layers. The ECAL is comprised of one barrel and two end-cap sectors employing liquid Argon (LAr). The showers hereby develop as electrons pairs which are then collected. The HCAL is also comprised of one barrel and two end-cap sectors. The sensors in the barrel of the HCAL are tiles of scintillating plastic whereas LAr is employed for the end-cap. A forward region, the closest possible to the beam, is covered by a LAr forward calorimeter (FCal). The LAr and Tile Calorimeter will be briefly discussed in the

565 following paragraphs.

566 The Liquid Argon Calorimeters

567 The ECAL is comprised of multiple layers of liquid Argon (LAr) sampler and lead ab-
568 sorber. The choice of its accordion-geometry design brought two main advantages; full
569 ϕ coverage with no non-interactive regions (no cracks); fast extraction of signals coming
570 from both front or rear end of the electrodes. It is made of two half-barrel wheels, both
571 placed in the barrel cryostat, that provide a pseudorapidity coverage up to $|\eta| < 1.475$
572 and two end-cap detectors providing $1.375 \leq |\eta| \leq 3.20$ coverage in two end-cap cryo-
573 stats. The junction between the barrel and end cap components defines the crack region
574 and any signal coming from the crack region is therefore discarded.

575 In the $|\eta| < 1.8$ region there is an additional layer, placed at the front of the calorimeter,
576 that is made of a thin (0.5 cm in the end-cap and 1.1 cm in the barrel) LAr layer with
577 no absorber [26]. This additional layer was designed to correct for the energy lost, as
578 particles enter the calorimeter, by taking a measurement just before the majority of the
579 electromagnetic shower is developed.

580 The Tile calorimeter

581 The main purpose of the hadronic calorimeter is to measure the energy of hadronic showers.
582 It is built employing steel and scintillating tiles coupled to optical fibres which are read
583 out by photo-multipliers. As shown in Figure 2.5, the HCAL is made up of three cylin-
584 ders; a central barrel, 5.64 m long covering a region $|\eta| < 1.0$, and two extended barrel,
585 2.91 m long covering a reigon $0.8 < |\eta| < 1.7$. Each cylinder is made up of 64 modules
586 and each module is in turn made up of three layers. Ultimately, the smallest section of the
587 calorimeter module is a cell with a $\Delta\phi \times \Delta\eta = 0.1 \times 0.1$ granularity for the two innermost
588 layers and $\Delta\phi \times \Delta\eta = 0.2 \times 0.1$ for the outermost one.

589 2.2.4 The Muon Spectrometer

590 The MS [27], shown in Figure 2.6, is the outermost sub-system of the whole ATLAS de-
591 tector. As such, it surrounds the calorimeters and its main function is to perform precision
592 measurement of muons momenta. The deflection of muon tracks employing large super-
593 conducting air-core toroid magnets and high-precision tracking chambers is at the heart
594 of such high precision measurement.

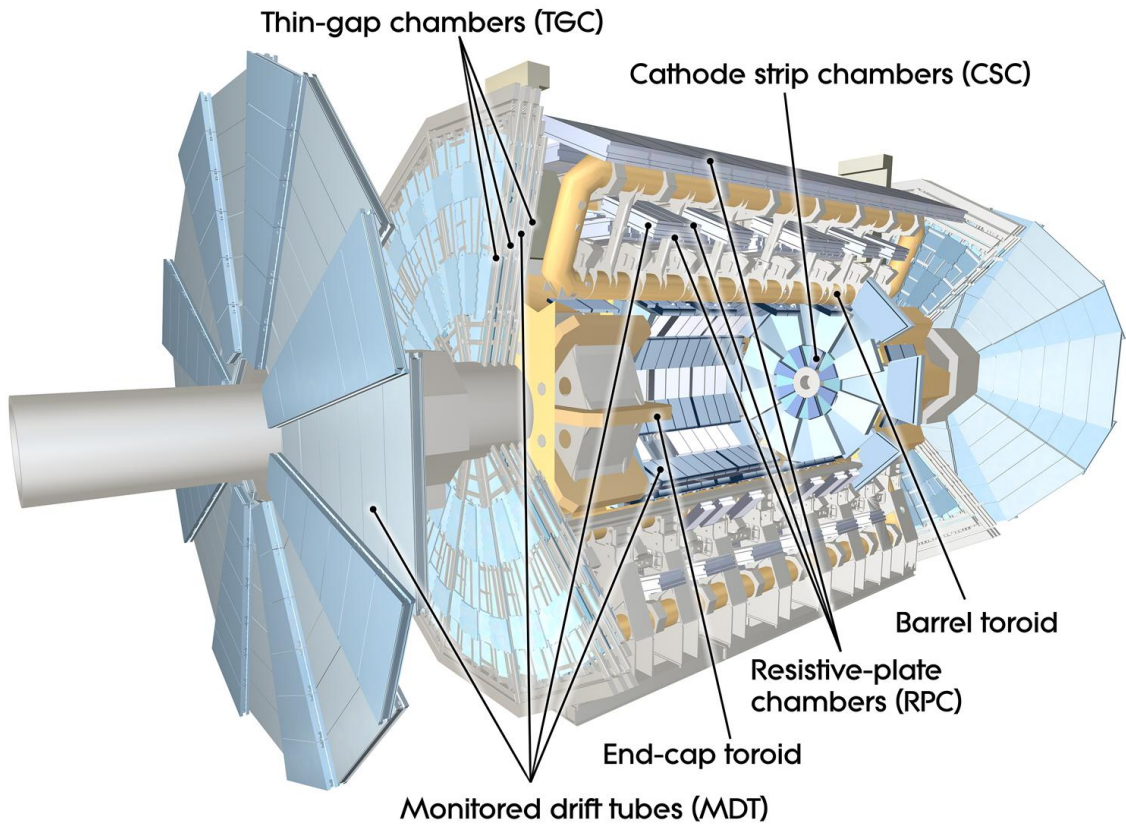


Figure 2.6: Cut-away view of the ATLAS muon system [3].

595 The MS is comprised of one large barrel toroid, covering the region $|\eta| \leq 1.4$, and
 596 two end-cap toroids, covering $1.6 < |\eta| \leq 2.7$ which are employed together to achieve the
 597 track-bending effect wanted. The magnitude of the magnetic field in the barrel, generated
 598 by eight large superconducting coils, ranges from 0.5 to 2 T.

599 Around the beam axis, three cylindrical layers make way for the chambers, placed in
 600 planes perpendicular to the beam, used to measure tracks.

601 Monitored Drift Chambers (MDTs) are employed over most of the pseudorapidity
 602 range to provide precision measurement of track coordinates in the bending direction.
 603 Cathode Strip Chambers (CSCs) are instead employed at large pseudorapidity ($2 < |\eta| <$
 604 2.7). Finally, in the end-cap regions Thin-Gap Chambers (TGCs) together with Resistive-
 605 Plate Chambers (RPCs) are dedicated to the Trigger System discussed in Section 2.3.

606 2.3 The ATLAS Trigger System

607 The ATLAS Trigger System is at the heart of data taking. It is an essential component of
 608 any nuclear or particle physics experiment since it is responsible for deciding whether or
 609 not to store an event for later study [4]. The ATLAS Trigger system is employed to reduce

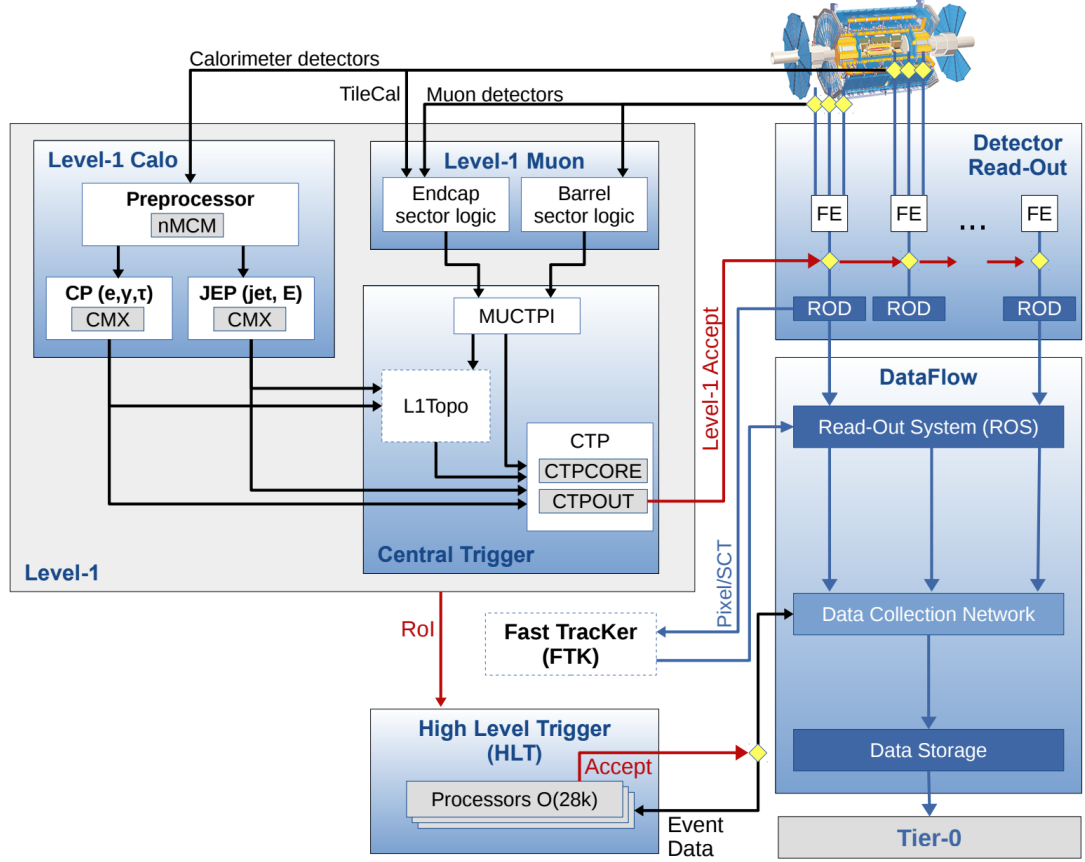


Figure 2.7: The ATLAS TDAQ system. L1Topo and FTK were being commissioned during 2015 and not used for the results shown in this thesis [4].

the event rate from $\sim 40 \text{ MHz}$ ¹ bunch-crossing² to $\sim 200 \text{ Hz}$ which corresponds to roughly 300 MB/s.

The Trigger and Data Acquisition (TDAQ) system shown in Figure 2.7 consists of a hardware-based first level trigger (L1) and a software-based high-level trigger (HLT). The L1 trigger decision is formed by the Central Trigger Processor (CTP), which receives inputs from the L1 calorimeter (L1Calo) and L1 muon (L1Muon) triggers. The first level (L1), which was designed to perform the first selection step, is a hardware-based system that uses information from the calorimeter and muon subdetectors. It also defines the so-called Regions of Interest (RoIs) within the detector to be investigated by the next level trigger, the HLT. Additionally, a Fast TracKer (FTK) system [28] (not yet installed) will provide global ID track reconstruction at the L1 trigger rate using lookup tables stored in

¹The LHC delivers beams with a bunch-spacing of 25 ns.

²The term bunch-crossing is hereby used when referring to a collision between two bunches of protons. Since only a certain fraction of the total momentum carried by each proton contributes to the collision, an average number of interactions per bunch-crossing, $\langle \mu \rangle$ is used.

621 custom associative memory chips for the pattern recognition. The FPGA-based track fitter
 622 will perform a fast linear fit and the tracks are made available to the HLT. This system will
 623 allow the use of tracks at much higher event rates in the HLT than is currently affordable
 624 using CPU systems. However, the upgrade of the ATLAS trigger will not be discussed
 625 any further.

626 In the next sections the L1 and HLT will be briefly described.

627 2.3.1 Level 1 Trigger

628 The Level 1 Trigger identifies Regions of Interest (RoIs)³ and passes these to HLT which
 629 will perform further investigations. Furthermore, in order to decide whether or not the
 630 event processing will continue, L1 selection uses only information coming from some
 631 parts of the detector to keep the input rate to a maximum of 100 kHz. L1 is implemented
 632 in fast custom electronics to keep the latency⁴ below 2.5 μ s. Event data from other sub-
 633 syststem are temporarily stored in memories whilst L1 decision is taken.

634 The L1 topological trigger (L1-Topo) [29] is feeded with energy and direction inform-
 635 ation, about the objects found by the L1 calorimeter and the muon trigger, which will be
 636 processed by dedicated algorithms implemented in its own FPGAs. However, due to the
 637 100 kHz read-out rate, not all the information collected by L1-Topo will be sent to the HLT,
 638 but only part of it. In order to properly seed the ROI-guided HLT reconstruction, specific
 639 objects in combination with the correct topological criteria must be employed.

640 2.3.2 High-Level Trigger

641 The HLT is used to reduce the output rate down to 1 kHz and it has a \sim 200 ms average
 642 decision time. Events that pass L1 trigger are then processed by the HLT using finer-
 643 granularity calorimeter information, precision measurements from the MS and tracking
 644 information from the ID. The HLT reconstruction can be run within RoIs identified at L1
 645 or a so-called full-scan on the full detector can be performed. The track reconstruction in
 646 the Inner Detector is an essential component of the trigger decision in the HLT and it will
 647 be discussed more in detail in Chapter 3

³ $\eta - \phi$ regions where event features have been found by the L1 selection process.

⁴Time needed by an electric signal to get to the front-end electronics.

648 **3** | The *b*-jet Trigger Signature in AT-
649 LAS

650 In this chapter the monitor and performance of the bottom-quark-initiated jet (*b*-jet) sig-
651 nature trigger, this being the author’s “technical/qualification task” to become a qualified
652 member of the experiment, will be discussed. The efficiencies of some of the Run 2 *b*-jet
653 triggers were evaluated using 3.8 fb^{-1} of pp collisions data collected in 2015 with 25 ns
654 bunch-spacing.

655 The qualification task

656 **3.1 Trigger Efficiency**

657 **4** | Event Simulation and Reconstruction

658

659 bla bla bla

660 **4.1 Event Generation**

661 bla bla

662 **4.1.1 Parton Distribution Functions (PDFs)**

663 bla bla bla

664 **4.1.2 Matrix Element Calculation**

665 bla bla bla

666 **4.1.3 Parton Showers**

667 bla bla bla

668 **4.1.4 Hadronisation**

669 bla bla bla

670 **4.2 Detector Simulation**

671 bla bla bla

672 **5**

| Stop searches in final states with
673 jets and missing transverse en-
674 ergy

675 **6** | Results and Statistical Interpretations

676

⁶⁷⁷ Trigger

⁶⁷⁸ bla vlas bla

Bibliography

- [1] ATLAS Collaboration, "Summary plots from the atlas standard model physics group." https://atlas.web.cern.ch/Atlas/GROUPS/PHYSICS/CombinedSummaryPlots/SM/ATLAS_a_SMSummary_TotalXsect/ATLAS_a_SMSummary_TotalXsect.png. viii, 9
- [2] C. Lefèvre, *The CERN accelerator complex.*, <http://cds.cern.ch/record/1260465>. viii, 16, 17
- [3] ATLAS Collaboration, *The ATLAS experiment at the CERN Large Hadron Collider*, Journal of Instrumentation **3** no. 08, (2008) S08003. <http://stacks.iop.org/1748-0221/3/i=08/a=S08003>. viii, 18, 24
- [4] A. Collaboration, *Performance of the ATLAS Trigger System in 2015*, Eur. Phys. J. **C77** (2017), [arXiv:1611.09661 \[hep-ex\]](arXiv:1611.09661). ix, 24, 25
- [5] M. Herrero, *The Standard Model.*, <https://arxiv.org/abs/hep-ph/9812242>. 3
- [6] ATLAS Collaboration, *Observation of a New Particle in the Search for the Standard Model Higgs Boson with the ATLAS Detector at the LHC*, Phys.Lett. **B716** (2012), [arXiv:1207.7214 \[hep-ex\]](arXiv:1207.7214). 3
- [7] CMS Collaboration, *Observation of a new boson at a mass of 125 GeV with the CMS experiment at the LHC*, Phys.Lett. **B716** (2012), [arXiv:1207.7235 \[hep-ex\]](arXiv:1207.7235). 3
- [8] A. Pich, *The Standard Model of Electroweak Interactions*, [arXiv:1201.0537 \[hep-ph\]](arXiv:1201.0537). 5, 6
- [9] K. A. Olive at al. (Particle Data Group), *Review of Particle Physics*, Chin.Phys. C **38(9)** (2014). 6
- [10] J. Goldstone, A. Salam and S. Weinberg, *Broken Symmetries*, Phys. Rev. **127** (1962) 965–970. 8

- 703 [11] S. Weinberg, *Implications of Dynamical Symmetry Breaking*, Phys. Rev. **D19** (1976)
 704 1277–1280. 10
- 705 [12] Super-Kamiokande Collaboration, Y. Fukuda et al., *Evidence for oscillation of*
 706 *atmospheric neutrinos*, Phys. Rev. Lett. **81** (1998) 1562–1567, arXiv:hep-ex/9807003
 707 [hep-ex]. 10
- 708 [13] SNO Collaboration, *Measurement of the Rate of $\nu_e + d \rightarrow p + p + e^-$ Interactions*
 709 *Produced by 8B Solar Neutrinos at the Sudbury Neutrino Observatory*, Phys. Rev. Lett.
 710 **87** (2001). 10
- 711 [14] T. O. W. of the Nobel Prize.
 712 https://www.nobelprize.org/nobel_prizes/physics/laureates/2015/. 10
- 713 [15] F. Jegerlehner, *The hierarchy problem of the electroweak Standard Model revisited*,
 714 arXiv:1305.6652 [hep-ph]. 12
- 715 [16] J.M. Jowett, M. Schaumann, R. Alemany, R. Bruce, M. Giovannozzi, P. Hermes, W.
 716 Hofle, M. Lamont, T. Mertens, S. Redaelli, J. Uythoven, J. Wenninger, *The 2015*
 717 *Heavy-Ion Run of the LHC*,
 718 <http://accelconf.web.cern.ch/accelconf/ipac2016/papers/tupmw027.pdf>. 15
- 719 [17] O. S. Brüuning, P. Collier, P. Lebrun, S. Myers, R. Ostojic, J. Poole and P. Proudlock,
 720 *LHC Design Report*, <https://cds.cern.ch/record/782076>. 16
- 721 [18] CMS Collaboration, *The CMS experiment at the CERN LHC*, Journal of
 722 Instrumentation **3** no. 08, (2008) S08004.
 723 <http://stacks.iop.org/1748-0221/3/i=08/a=S08004>. 16
- 724 [19] LHCb Collaboration, et. al, *The LHCb Detector at the LHC*, JINST (2008). 16
- 725 [20] ALICE Collaboration, *The ALICE experiment at the CERN LHC*, Journal of
 726 Instrumentation **3** no. 08, (2008) S08002.
 727 <http://stacks.iop.org/1748-0221/3/i=08/a=S08002>. 16
- 728 [21] A. Yamamoto, Y. Makida, R. Ruber, Y. Doi, T. Haruyama, F. Haug, H. ten Kate,
 729 M. Kawai, T. Kondo, Y. Kondo, J. Metselaar, S. Mizumaki, G. Olesen, O. Pavlov,
 730 S. Ravat, E. Sbrissa, K. Tanaka, T. Taylor, and H. Yamaoka, *The ATLAS central*
 731 *solenoid*, Nuclear Instruments and Methods in Physics Research Section A:
 732 Accelerators, Spectrometers, Detectors and Associated Equipment **584** no. 1, (2008)

- 733 53 – 74.
- 734 <http://www.sciencedirect.com/science/article/pii/S0168900207020414>. 18,
- 735 19
- 736 [22] ATLAS Collaboration, *The ATLAS Inner Detector commissioning and calibration*, *Eur. Phys. J.* **C70**, [arXiv:1004.5293](https://arxiv.org/abs/1004.5293). 19
- 738 [23] ATLAS Collaboration, *ATLAS Insertable B-Layer Technical Design Report*,
739 <https://cds.cern.ch/record/1291633>. 20
- 740 [24] G. A. et al., *ATLAS pixel detector electronics and sensors*, *Journal of Instrumentation* **3**
741 no. 07, (2008) P07007. <http://stacks.iop.org/1748-0221/3/i=07/a=P07007>. 21
- 742 [25] A. Bingül, *The ATLAS TRT and its Performance at LHC*, *Journal of Physics: Conference Series* **347** no. 1, (2012) 012025.
743 <http://iopscience.iop.org/article/10.1088/1742-6596/347/1/012025/meta>.
744 21
- 745 [26] ATLAS Collaboration, *ATLAS liquid-argon calorimeter: Technical Design Report*,
746 <https://cds.cern.ch/record/331061>. 23
- 748 [27] ATLAS Collaboration, *ATLAS muon spectrometer: Technical design report*,
749 <https://cds.cern.ch/record/331068>. 23
- 750 [28] ATLAS Collaboration, *Fast TracKer (FTK) Technical Design Report*,
751 <https://cds.cern.ch/record/1552953>. 25
- 752 [29] E. Simoni, *The Topological Processor for the future ATLAS Level-1 Trigger: from design to
753 commissioning*, [arXiv:1406.4316](https://arxiv.org/abs/1406.4316). 26